Structural Engineering and Mechanics, *Vol. 61, No. 4 (2017) 551-561*
DOI: https://doi.org/10.12989/sem.2017.61.4.551

An approximate spectral element model for the dynamic analysis of an FGM bar in axial vibration

Minsik Lee[a], Ilwook Park[b] and Usik Lee[*]

Department of Mechanical Engineering, Inha University, Inha-ro 100, Nam-gu, Incheon 22212, Republic of Korea

(Received June 28, 2016, Revised December 27, 2016, Accepted January 18, 2017)

Abstract. As FGM (functionally graded material) bars which vibrate in axial or longitudinal direction have great potential for applications in diverse engineering fields, developing a reliable mathematical model that provides very reliable vibration and wave characteristics of a FGM axial bar, especially at high frequencies, has been an important research issue during last decades. Thus, as an extension of the previous works (Hong *et al.* 2014, Hong and Lee 2015) on three-layered FGM axial bars (hereafter called FGM bars), an enhanced spectral element model is proposed for a FGM bar model in which axial and radial displacements in the radial direction are treated more realistic by representing the inner FGM layer by multiple sub-layers. The accuracy and performance of the proposed enhanced spectral element model is evaluated by comparison with the solutions obtained by using the commercial finite element package ANSYS. The proposed enhanced spectral element model is also evaluated by comparison with the author's previous spectral element model. In addition, the effects of Poisson's ratio on the dynamics and wave characteristics in example FGM bars are numerically investigated.

Keywords: functionally graded material (FGM); three-layered FGM axial bar; spectral element method; dynamic responses; waves

1. Introduction

Material properties of functionally graded materials (FGMs) can be designed to vary in spatial coordinates in order to achieve the desired mechanical, thermal, and/or electrical functions. It is well recognized that FGMs can help reduce the residual stresses and stress concentrations at the interfaces between two dissimilar materials and also can help improve the strength and toughness of a structure. Thus, as one of the most advanced composite materials, FGMs have recently received a considerable attention in various engineering fields including the mechanical, automobile, aerospace, electronics, biomedical, and defense industries.

Various types of FGM structures have been investigated and reported in the literature: they include axial bars (Maalawi 2011), torsional bars (Horgan 2007), beams (Chakraborty and Gopalakrishinan 2003, Kutis and Murin 2006, Xiang and Yang 2008, Yu and Chu 2009, Huang and Li 2010, Shahba *et al.* 2011, Menaa *et al.* 2012, Murin *et al.* 2013, Nguyen 2013, Pradhan and Chakraverty 2013, Mashat *et al.* 2014, Murin *et al.* 2016), plates (Parker 2009), annular circular plates or disks (Efraim and Eisenberger 2007, Horgan 1999), and electro-thermo and electro-thermo-structural problems (Murin *et al.* 2008, Murin *et al.* 2011). For most one-dimensional (1-D) FGM structures, the material properties have been assumed to vary in the axial direction (Kutis and Murin 2006, Huang and Li 2010, Maalawi 2011, Shahba *et al.* 2011), in the thickness (or radial) direction (Chakraborty and Gopalakrishinan 2003, Horgan 2007, Yu and Chu 2009, Menaa *et al.* 2012), or in both the axial and thickness directions (Xiang and Yang 2008, Murin *et al.* 2011, Murin *et al.* 2013, Murin *et al.* 2016). An excellent extensive review of the present state of the art in static and dynamic analyses of the FGM beams is referred to Murin *et al.* (2016). In this study, the discussion will be limited to the axial bars made of FGMs that deform in the axial or longitudinal direction with lateral contractions.

For static and dynamic analysis of FGM structures, various analytical and numerical methods have been applied including analytical methods (Horgan 1999, Horgan 2007, Parker 2009, Menaa 2012, Nguyen 2013), Rayleigh-Ritz method (Pradhan and Chakraverty 2013), power series expansion methods (Huang and Li 2010, Maalawi 2011), differential quadrature methods (Xiang and Yang 2008), Mathematica (Murin *et al.* 2013), dynamic stiffness methods (Efraim and Eisenberger 2007), finite element methods (FEM) (Kutis and Murin 2006, Murin *et al.* 2008, Yu and Chu 2009, Murin *et al.* 2011, Shahba *et al.* 2011, Mashat *et al.* 2014, Murin *et al.* 2016,), and spectral element methods (SEM) (Lee 2009, Chakraborty and Gopalakrishinan 2003, Hong *et al.* 2014, Hong and Lee 2015). Recently, Murin *et al.* (2016) developed a beam finite element for the FGM beams with a double symmetric cross-section and they showed that the beam finite element is very accurate and effective because the spatial variation

∗Corresponding author, Professor
E-mail: ulee@inha.ac.kr
[a]MSc Student
E-mail: mslee89@inha.edu
[b]MSc Student
E-mail: iwpark@inha.edu

ISSN: 1225-4568 (Print), 1598-6217 (Online)

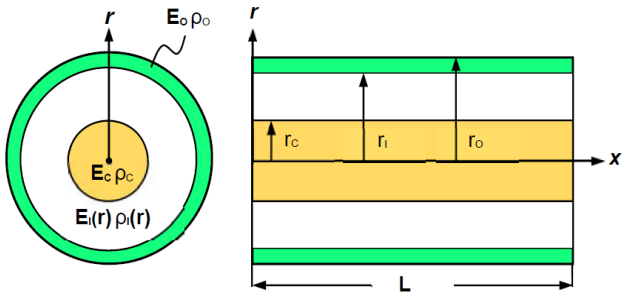

Fig. 1 Geometric and material properties of a three-layered FGM bar (Hong and Lee 2015)

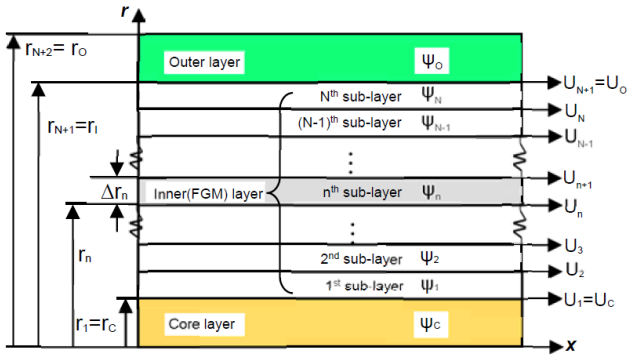

Fig. 2 Sub-layers in the inner FGM layer of a three-layered FGM bar

of material properties can be modelled with only one finite element.

The FEM is one of most powerful computational methods that can be applied to complex structural engineering problems such as the FGM structures. To formulate standard finite element models, simple polynomials that are independent of the vibrating frequency are normally used as interpolation functions. Thus, as a drawback to the FEM, many very fine meshes are required to obtain sufficiently accurate FEM solutions, especially in the high frequency regime. This significantly increases the required number of degrees of freedom (DOFs) and greatly increases the computation time and cost. In contrast to the standard FEM, the frequency domain spectral element method (SEM) is well-recognized as an exact element method that provides extremely accurate solutions, even at very high frequencies, by using only a minimum number of DOFs. This approach significantly reduces the computation time and cost. This is true for the SEM because frequency-dependent interpolation functions derived from exact free wave solutions are used to formulate an exact dynamic stiffness matrix (often called the spectral element matrix) that is used in SEM as the finite element stiffness matrix (Lee 2009). Despite the aforementioned advantages of SEM, there have been very few applications to FGM structures (Chakraborty and Gopalakrishinan 2003, Hong *et al.* 2014, Hong and Lee 2015).

FGM axial bars are 1-D structures that deform mainly in the axial or longitudinal direction with lateral contractions and they have great potential for applications in many engineering fields. However, to the authors' best knowledge there have been very few studies on the FGM axial bars. Maalawi (2011) presented analytical solutions for an FGM axial bar whose material properties vary in the axial direction. Hong *et al.* (2014) and Hong and Lee (2015) applied the SEM to three-layered FGM axial bars (hereafter called an FGM bar) that consist of three layers: the core, the inner FGM layer, and the outer layer. The core and outer layer are made of metals and the inner FGM layer is made of FGM. The material properties of the inner FGM layer were assumed to vary in the radial direction satisfying the power law (Markworth *et al.* 1995).

In Hong *et al.* (2014), the axial displacement was assumed to be uniform over the whole cross-section of an FGM bar, while the radial displacement over the whole cross-section was assumed to vary linearly in the radial direction. Later, Hong and Lee (2015) modified their previous model by relaxing the assumption made regarding the radial displacements: they assumed that the radial displacements in the core, inner layer, and outer layer can vary linearly, but independently, in the radial direction. However, the modified model considered in Hong and Lee (2015) does not seem fully realistic because the axial and radial displacements in the inner FGM layer might not necessarily vary linearly in the radial direction due to the radial variation of the material properties of the inner FGM layer.

Thus, the contributions of this study are (1) to develop a mathematical model for an FGM axial bar by taking into account more realistic axial and radial displacements in the inner FGM layer; (2) to develop an enhanced spectral element model for the FGM axial bar model; and (3) to evaluate the performance of the present model compared with previous models.

2. Governing equations of motion

The geometry of an axisymmetric FGM bar is shown in Fig. 1. The axial and radial coordinates are represented by x and r, respectively. The FGM bar consists of three layers of different materials. The core ($0 \le r \le r_C$) and the outer layer ($r_I \le r \le r_O$) are made of isotropic metals, and the inner FGM layer ($r_C \le r \le r_I$) is made of an FGM whose material properties vary in the radial direction. In this paper, the subscripts C, I, and O are used to denote quantities for the core layer, the inner FGM layer, and the outer layer, respectively. For example, r_C, r_I, and r_O represent the radii of the core, the inner FGM layer, and the outer layer, respectively.

It is assumed that the axial displacements in the core and the outer layer are uniform over the cross-section, while the radial displacements due to lateral contraction vary linearly in the radial direction. However, in contrast to previous models described in Hong *et al.* (2014) and Hong and Lee (2015), the axial and radial displacements in the inner FGM layer are assumed not to necessarily vary linearly in the radial direction due to the variation of the FGM properties in the radial direction.

Accordingly the inner FGM layer is divided into N sub-layers as shown in Fig. 2. In Fig. 2, $U_C(x,t)$ and $U_O(x,t)$ are

the axial displacements in the core and the outer layer, respectively. Similarly $\psi_C(x,t)$ and $\psi_O(x,t)$ are the functions for the lateral contractions in the core and the outer layer, respectively. The axial displacements at the interfaces of each layer are denoted by $U_n(x,t)$ (n = 1, 2, …, N+1) and the lateral contractions are denoted by the functions $\psi_n(x,t)$ (n = 1, 2, …, N).

The displacement fields in the three layers of the FGM bar can be expressed in the following forms

$$\begin{aligned} &u_C(x,r,t) = U_C(x,t) = U_1(x,t) \\ &v_C(x,r,t) = r\psi_C(x,t) \end{aligned} \quad (0 \le r \le r_C)$$

$$\begin{aligned} &u_I(x,r,t) = \boldsymbol{R}_{uI}(r)\boldsymbol{u}(x,t) \\ &v_I(x,r,t) = \boldsymbol{R}_{vI}(r)\boldsymbol{\psi}(x,t) \end{aligned} \quad (r_C \le r \le r_I)$$

$$\begin{aligned} &u_O(x,r,t) = U_O(x,t) = U_{N+1}(x,t) \\ &v_O(x,r,t) = \boldsymbol{R}_{vO}(r)\boldsymbol{\psi}(x,t) \end{aligned} \quad (r_I \le r \le r_O) \tag{1}$$

where

$$\begin{aligned} &\boldsymbol{u}(x,t) = \{U_1(x,t) \quad U_2(x,t) \quad \cdots \quad U_N(x,t) \quad U_{N+1}(x,t)\}^{\mathrm{T}} \\ &\boldsymbol{\psi}(x,t) = \{\psi_C(x,t) \quad \psi_1(x,t) \quad \psi_2(x,t) \quad \cdots \quad \psi_N(x,t) \quad \psi_O(x,t)\}^{\mathrm{T}} \end{aligned} \tag{2}$$

and

$$\begin{aligned} &\boldsymbol{R}_{uI}(r) = [R_1(r) \quad R_2(r) \quad \cdots \quad R_N(r) \quad R_{(N+1)}(r)] \\ &\boldsymbol{R}_{vI}(r) = \boldsymbol{H}(r)\boldsymbol{\Delta}(r) \\ &\boldsymbol{R}_{vO}(r) = [\Delta r_0 \quad \Delta r_1 \quad \Delta r_2 \quad \cdots \quad \Delta r_N \quad (r - r_{N+1})] \end{aligned} \tag{3}$$

In Eq. (3), the following definitions are used

$$R_1 = \frac{r - r_2}{r_1 - r_2} H_1(r)$$

$$R_{(N+1)} = \frac{r - r_N}{r_{N+1} - r_N} H_N(r)$$

$$R_n = \frac{r - r_{n-1}}{r_n - r_{n-1}} H_{n-1}(r) + \frac{r - r_{n+1}}{r_n - r_{n+1}} H_n(r), \quad (n = 2,3,\cdots,N) \tag{4}$$

$$\boldsymbol{H}(r) = [H_1(r) \quad H_2(r) \quad \cdots \quad H_N(r)]_{(1\times N)}$$

$$\boldsymbol{\Delta}(r) = \begin{bmatrix} \Delta r_0 & (r - r_1) & 0 & 0 & \cdots & 0 & 0 \\ \Delta r_0 & \Delta r_1 & (r - r_2) & 0 & \cdots & 0 & 0 \\ \Delta r_0 & \Delta r_1 & \Delta r_2 & (r - r_3) & \cdots & 0 & 0 \\ \vdots & \vdots & \vdots & \vdots & \ddots & \vdots & \vdots \\ \Delta r_0 & \Delta r_1 & \Delta r_2 & \Delta r_3 & \cdots & (r - r_N) & 0 \end{bmatrix}$$

where

$$\begin{aligned} &H_n(r) = h(r - r_n) - h(r - r_{n+1}) \\ &\Delta r_n = r_{n+1} - r_n \quad (n = 0,1,2,\cdots,N;\ r_0 = 0) \end{aligned} \tag{5}$$

and where $h(r)$ is the Heaviside step function (Kreyszig 1972). Note that the displacement fields in Eq. (1) fully satisfy the displacement connectivity at all interfaces between the three layers and the sub-layers in the inner layer.

The constitutive relations for each elastic layer are given by (Hong and Lee 2015)

$$\begin{Bmatrix} \sigma_{xx}^{(i)} \\ \sigma_{rr}^{(i)} \\ \sigma_{\theta\theta}^{(i)} \\ \tau_{xr}^{(i)} \end{Bmatrix} = \begin{bmatrix} \lambda_i + 2\mu_i & \lambda_i & \lambda_i & 0 \\ \lambda_i & \lambda_i + 2\mu_i & \lambda_i & 0 \\ \lambda_i & \lambda_i & \lambda_i + 2\mu_i & 0 \\ 0 & 0 & 0 & \mu_i \end{bmatrix} \begin{Bmatrix} \varepsilon_{xx}^{(i)} \\ \varepsilon_{rr}^{(i)} \\ \varepsilon_{\theta\theta}^{(i)} \\ \gamma_{xr}^{(i)} \end{Bmatrix} \quad (i = \mathrm{C, I, O}) \tag{6}$$

where σ_{xx}, σ_{rr}, and $\sigma_{\theta\theta}$ are normal stresses in the axial, radial, and circumferential directions, respectively, and τ_{xr} is the shear stress. Similarly ε_{xx}, ε_{rr}, and $\varepsilon_{\theta\theta}$ are normal stresses in the axial, radial, and circumferential directions, respectively, and γ_{xr} is the shear strain. The subscript θ denotes the circumferential direction. λ_i and μ_i (i=C, I, O) are the Lamé constants, which are assumed to be constant in the core and the outer layer, but to vary in the inner FGM layer as follows

$$\lambda_I(r) = \frac{E_I(r)\nu_I}{(1-2\nu_I)(1+\nu_I)}, \quad \mu_I(r) = \frac{E_I(r)}{2(1+\nu_I)} \tag{7}$$

The inner FGM layer is made by mixing two materials of the core and outer layer. Thus, we assumed that the Young's modulus $E_I(r)$ and the mass density $\rho_I(r)$ of the inner FGM layer are determined by blending the material properties of the core and outer layer smoothly according to the power law (Markworth *et al.* 1995)

$$\begin{aligned} E_I(r) &= (E_O - E_C)\left(\frac{r - r_C}{r_I - r_C}\right)^m + E_C, \\ \rho_I(r) &= (\rho_O - \rho_C)\left(\frac{r - r_C}{r_I - r_C}\right)^m + \rho_C \end{aligned} \tag{8}$$

where m is the power law exponent. As discussed by Li (2008), the continuous variation of material properties, given by Eq. (8) for instance, can be achieved by gradually changing the volume fraction of the constituent materials by using some special manufacturing methods such as high-speed centrifugal casting, power metallurgy methods, etc. The Poisson's ratios in the core, the inner FGM layer, and the outer layer are denoted by ν_C, ν_I, and ν_O, respectively. In this study, we assumed that the Poisson's ratio in the inner FGM layer does not vary in the radial direction: this assumption can simplify the theoretical formulation described in the following. Extension to the case of the FGM layer with varying Poisson's ratio will be made in the future work.

The strains in each layer can be readily obtained from

$$\varepsilon_{xx}^{(i)} = \frac{\partial u_i}{\partial x}, \quad \varepsilon_{rr}^{(i)} = \frac{\partial v_i}{\partial r}, \quad \varepsilon_{\theta\theta}^{(i)} = \frac{v_i}{r}, \quad \gamma_{xr}^{(i)} = \frac{\partial u_i}{\partial r} + \frac{\partial v_i}{\partial x} \quad (i = \mathrm{C, I, O}) \tag{9}$$

The equations of motion of the axial bar can be derived from Hamilton's principle given by (Meirovitch 1967)

$$\int_{t_1}^{t_2} (\delta T - \delta U + \delta W)\, dt = 0 \tag{10}$$

where δT and δU denote the variations of the kinetic energy T and the potential energy U, respectively, and δW is the

virtual work done by external forces.

By using the displacement fields given by Eq. (1), the kinetic energy T stored in an axial bar element of length l can be derived as follows

$$\begin{aligned} T &= \sum_{i=C,I,O} \int_0^l \int_A \frac{1}{2}(\rho_i \dot{u}_i^2 + \rho_i \dot{v}_i^2)\, dA dx \\ &= \frac{1}{2}\int_0^l [\dot{\boldsymbol{u}}^{\mathrm{T}}(x,t)\boldsymbol{M}_{uu}\dot{\boldsymbol{u}}(x,t) + \dot{\boldsymbol{\psi}}^{\mathrm{T}}(x,t)\boldsymbol{M}_{\psi\psi}\dot{\boldsymbol{\psi}}(x,t)]dx \end{aligned} \tag{11}$$

where ρ_i (i=C, I, O) are the mass densities of each layer and the dots ($\cdot$) denote derivatives with respect to time t. The effective mass matrices $\boldsymbol{M}_{uu}$ and $\boldsymbol{M}_{\psi\psi}$ are defined in Appendix A. Similarly the strain energy U can be derived as follows

$$\begin{aligned} U &= \sum_{i=C,I,O} \int_0^l \int_A \frac{1}{2}(\sigma_{xx}^{(i)}\varepsilon_{xx}^{(i)} + \sigma_{rr}^{(i)}\varepsilon_{rr}^{(i)} + \sigma_{\theta\theta}^{(i)}\varepsilon_{\theta\theta}^{(i)} + \tau_{xr}^{(i)}\gamma_{xr}^{(i)})\, dA dx \\ &= \frac{1}{2}\int_0^l [\boldsymbol{u}_{,x}^{\mathrm{T}}(x,t)\boldsymbol{K}_{u'u'}\boldsymbol{u}_{,x}(x,t) + \boldsymbol{u}^{\mathrm{T}}(x,t)\boldsymbol{K}_{uu}\boldsymbol{u}(x,t) + 2\boldsymbol{u}_{,x}^{\mathrm{T}}(x,t)\boldsymbol{K}_{u'\psi}\boldsymbol{\psi}(x,t) \\ &\quad + 2\boldsymbol{\psi}_{,x}^{\mathrm{T}}(x,t)\boldsymbol{K}_{\psi'u}\boldsymbol{u}(x,t) + \boldsymbol{\psi}_{,x}^{\mathrm{T}}(x,t)\boldsymbol{K}_{\psi'\psi'}\boldsymbol{\psi}_{,x}(x,t) + \boldsymbol{\psi}^{\mathrm{T}}(x,t)\boldsymbol{K}_{\psi\psi}\boldsymbol{\psi}(x,t)]dx \end{aligned} \tag{12}$$

where the symbols $(\ )_{,x}$ denote the derivatives with respect to the axial coordinate x, and the effective stiffness matrices $\boldsymbol{K}_{u'u'}$, $\boldsymbol{K}_{uu}$, $\boldsymbol{K}_{u'\psi}$, $\boldsymbol{K}_{\psi'u}$, $\boldsymbol{K}_{\psi'\psi'}$, and $\boldsymbol{K}_{\psi\psi}$ are defined in Appendix A. Finally, the virtual work done by all external forces can be derived as follows

$$\begin{aligned} \delta W = \int_0^l q(x,t)\delta U_O dx &+ \boldsymbol{N}_1^{\mathrm{T}}(t)\delta\boldsymbol{u}(0,t) + \boldsymbol{N}_2^{\mathrm{T}}(t)\delta\boldsymbol{u}(l,t) \\ &+ \boldsymbol{T}_1^{\mathrm{T}}(t)\delta\boldsymbol{\psi}(0,t) + \boldsymbol{T}_2^{\mathrm{T}}(t)\delta\boldsymbol{\psi}(l,t) \end{aligned} \tag{13}$$

where $q(x,t)$ is the distributed axial force acting on the outer surface of the axial bar, $\boldsymbol{N}_1(t)$ and $\boldsymbol{N}_2(t)$ are the externally applied axial forces associated with $\boldsymbol{u}(x,t)$ at x=0 and x=l, respectively, and $\boldsymbol{T}_1(t)$ and $\boldsymbol{T}_2(t)$ are the externally applied forces associated with $\boldsymbol{\psi}(x,t)$ at x=0 and x=l respectively.

By substituting Eqs. (11)-(13) into Hamilton's principle given by Eq. (10) and performing some mathematical manipulations including integration-by-parts, we can derive the equations of motion for a uniform axial bar as follows

$$\begin{aligned} &\boldsymbol{K}_2\boldsymbol{w}_{,xx}(x,t) + (\boldsymbol{K}_1 - \boldsymbol{K}_1^{\mathrm{T}})\boldsymbol{w}_{,x}(x,t) \\ &- \boldsymbol{K}_0\boldsymbol{w}(x,t) - \boldsymbol{M}\ddot{\boldsymbol{w}}(x,t) + \boldsymbol{q}(x,t) = \boldsymbol{0} \end{aligned} \tag{14}$$

where

$$\boldsymbol{w}(x,t) = \begin{Bmatrix} \boldsymbol{u}(x,t) \\ \boldsymbol{\psi}(x,t) \end{Bmatrix}, \qquad \boldsymbol{q}(x,t) = \begin{Bmatrix} \boldsymbol{q}_u(x,t) \\ \boldsymbol{0} \end{Bmatrix} \tag{15}$$

and

$$\begin{aligned} \boldsymbol{K}_0 &= \begin{bmatrix} \boldsymbol{K}_{uu} & \boldsymbol{0} \\ \boldsymbol{0} & \boldsymbol{K}_{\psi\psi} \end{bmatrix}, \quad \boldsymbol{K}_1 = \begin{bmatrix} \boldsymbol{0} & \boldsymbol{K}_{u'\psi} \\ \boldsymbol{K}_{\psi'u} & \boldsymbol{0} \end{bmatrix} \\ \boldsymbol{K}_2 &= \begin{bmatrix} \boldsymbol{K}_{u'u'} & \boldsymbol{0} \\ \boldsymbol{0} & \boldsymbol{K}_{\psi'\psi'} \end{bmatrix}, \quad \boldsymbol{M} = \begin{bmatrix} \boldsymbol{M}_{uu} & \boldsymbol{0} \\ \boldsymbol{0} & \boldsymbol{M}_{\psi\psi} \end{bmatrix} \end{aligned} \tag{16}$$

where $\boldsymbol{q}_u(x,t)$={0 0 0 … 0 0 $q(x,t)$}$^{\mathrm{T}}$ is an (N+1)-by-one vector.

The natural and geometric boundary conditions associated with the preceding equations of motion are given by

$$\begin{aligned} &\boldsymbol{N}(0,t) = -\boldsymbol{N}_1(t) \text{ or } \boldsymbol{u}(0,t) = \boldsymbol{u}_1(t), \\ &\boldsymbol{T}(0,t) = -\boldsymbol{T}_1(t) \text{ or } \boldsymbol{\psi}(0,t) = \boldsymbol{\psi}_1(t), \\ &\boldsymbol{N}(l,t) = \boldsymbol{N}_2(t) \text{ or } \boldsymbol{u}(l,t) = \boldsymbol{u}_2(t) \\ &\boldsymbol{T}(l,t) = \boldsymbol{T}_2(t) \text{ or } \boldsymbol{\psi}(l,t) = \boldsymbol{\psi}_2(t) \end{aligned} \tag{17}$$

where $\boldsymbol{N}(x,t)$ and $\boldsymbol{T}(x,t)$ are the resultant forces defined by

$$\begin{aligned} \boldsymbol{N}(x,t) &= \boldsymbol{K}_{u'u'}\boldsymbol{u}_{,x}(x,t) + \boldsymbol{K}_{u'\psi}\boldsymbol{\psi}(x,t) \\ \boldsymbol{T}(x,t) &= \boldsymbol{K}_{\psi'u}\boldsymbol{u}(x,t) + \boldsymbol{K}_{\psi'\psi'}\boldsymbol{\psi}_{,x}(x,t) \end{aligned} \tag{18}$$

3. Spectral element modeling and analysis

3.1 Formulation of spectral element model

The spectral element of a uniform axial bar can be formulated by following the general procedure introduced in Lee (2009). In the first step of the spectral element formulation, we transform the time domain equations of motion into the frequency domain by representing all displacement fields and forcing terms in spectral forms by using discrete Fourier transform theory (Newland 1993) as follows

$$\begin{aligned} &\{\boldsymbol{w}(x,t),\, \boldsymbol{q}(x,t)\}^{\mathrm{T}} = \\ &\frac{1}{N_{DFT}} \sum_{n=0}^{N_{DFT}-1} \{\boldsymbol{W}_n(x;\omega)e^{i\omega_n t}, \boldsymbol{Q}_n(x;\omega)e^{i\omega_n t}\}^{\mathrm{T}} \end{aligned} \tag{19}$$

where $i = \sqrt{-1}$ is the imaginary unit, ω_n are the discrete frequencies, and $N_{DFT}/2$ is the number of spectral components up to the Nyquist frequency (Newland 1993). The subscripts n denote spectral components of the corresponding time-domain quantity and they will be omitted hereafter for the sake of brevity. By substituting Eq. (19) into Eq. (14), we obtain the frequency-domain governing equations

$$\boldsymbol{K}_2\boldsymbol{W}'' + (\boldsymbol{K}_1 - \boldsymbol{K}_1^{\mathrm{T}})\boldsymbol{W}' - (\boldsymbol{K}_0 - \omega^2\boldsymbol{M})\boldsymbol{W} + \boldsymbol{Q}(x) = \boldsymbol{0} \tag{20}$$

Free wave solutions can be obtained from homogeneous governing equations which can be readily reduced from Eq. (20) by removing external forcing terms (i.e., $\boldsymbol{Q}$=$\boldsymbol{0}$) as follows

$$\boldsymbol{K}_2\boldsymbol{W}'' + (\boldsymbol{K}_1 - \boldsymbol{K}_1^{\mathrm{T}})\boldsymbol{W}' - (\boldsymbol{K}_0 - \omega^2\boldsymbol{M})\boldsymbol{W} = \boldsymbol{0} \tag{21}$$

We can assume a free wave solution in the following form

$$\boldsymbol{W}(x;\omega) = \boldsymbol{r}ae^{-ikx} \tag{22}$$

By substituting Eq. (22) into Eq. (21), we obtain an eigenvalue problem as

$$[k^2\boldsymbol{K}_2 + ik(\boldsymbol{K}_1 - \boldsymbol{K}_1^{\mathrm{T}}) + (\boldsymbol{K}_0 - \omega^2\boldsymbol{M})]\boldsymbol{r} = 0 \tag{23}$$

From Eq. (23), we can compute wavenumbers (eigenvalues) and wave mode vectors (eigenvectors) simultaneously by using the MATLAB® function *polyeig* (MATLAB 1993) as follows

$$[\boldsymbol{R}(\omega),\boldsymbol{k}(\omega)] = \text{polyeig}\ \ [(\boldsymbol{K}_0 - \omega^2\boldsymbol{M}),\ i(\boldsymbol{K}_1 - \boldsymbol{K}_1^{\mathrm{T}}),\ \boldsymbol{K}_2] \tag{24}$$

where

$$\begin{aligned} \boldsymbol{R}(\omega) &= [\boldsymbol{r}_1 \quad \boldsymbol{r}_2 \quad \boldsymbol{r}_3 \quad \cdots \quad \boldsymbol{r}_{(4N+6)}] \\ \boldsymbol{k}(\omega) &= \{k_1 \quad k_2 \quad k_3 \quad \cdots \quad k_{(4N+6)}\} \end{aligned} \tag{25}$$

where $\boldsymbol{r}_i$ is the ith eigenvector corresponding to the ith wavenumber k_i, and N is the number of sub-layers in the inner FGM layer.

By using the wavenumbers k_i and wave mode vectors $\boldsymbol{r}_i$ (i = 1, 2, 3,…, 4N+6), we can write the free wave solution of Eq. (21) as

$$\boldsymbol{W}(x;\omega) = \boldsymbol{R}\boldsymbol{E}(x;\omega)\boldsymbol{a} \tag{26}$$

where $\boldsymbol{a}$ is a (4N+6)-by-one constant vector defined by

$$\boldsymbol{a} = \{\, a_1 \quad a_2 \quad a_3 \quad \cdots \quad a_{(4N+6)}\}^{\mathrm{T}} \tag{27}$$

and $\boldsymbol{E}(x;\omega)$ is a (4N+6)-by-(4N+6) diagonal matrix defined by

$$\boldsymbol{E}(x;\omega) = diagonal[e^{-ikx}] \quad (j = 1,\ 2,\ 3,\ldots,\ 4N+6) \tag{28}$$

We define the spectral components of the nodal degrees of freedom (DOFs) (or simply the spectral nodal DOFs) vector as

$$\boldsymbol{d} = \begin{Bmatrix} \boldsymbol{W}(0;\omega) \\ \boldsymbol{W}(l;\omega) \end{Bmatrix} = \begin{Bmatrix} \boldsymbol{W}_1(\omega) \\ \boldsymbol{W}_2(\omega) \end{Bmatrix} \tag{29}$$

By substituting Eq. (26) into Eq. (29), we can write the spectral nodal DOFs vector as

$$\boldsymbol{d} = \boldsymbol{H}(\omega)\boldsymbol{a} \tag{30}$$

where

$$\boldsymbol{H}(\omega) = \begin{bmatrix} \boldsymbol{R}\boldsymbol{E}(0;\omega) \\ \boldsymbol{R}\boldsymbol{E}(l;\omega) \end{bmatrix} \tag{31}$$

By using Eq. (30), the constant vector $\boldsymbol{a}$ from Eq. (26) is removed to obtain the following expression

$$\boldsymbol{W}(x;\omega) = \boldsymbol{R}\boldsymbol{E}(x;\omega)\,\boldsymbol{H}(\omega)^{-1}\boldsymbol{d} \tag{32}$$

or

$$\boldsymbol{W}(x;\omega) = \boldsymbol{N}(x;\omega)\boldsymbol{d} \tag{33}$$

where $\boldsymbol{N}(x;\omega)$ is the frequency-dependent dynamic shape function matrix defined by

$$\boldsymbol{N}(x;\omega) = \boldsymbol{R}\boldsymbol{E}(x;\omega)\,\boldsymbol{H}(\omega)^{-1} \tag{34}$$

To formulate the spectral element model by using the variational approach (Lee 2009), we derive the weak form of the original governing equations as follows

$$\begin{aligned} &\int_0^l \delta\boldsymbol{W}^{\mathrm{T}}[\boldsymbol{K}_2\boldsymbol{W}'' + (\boldsymbol{K}_1 - \boldsymbol{K}_1^{\mathrm{T}})\boldsymbol{W}' - (\boldsymbol{K}_0 - \omega^2\boldsymbol{M})\boldsymbol{W} + \boldsymbol{Q}]dx \\ &= -\int_0^l [\delta\boldsymbol{W}'^{\mathrm{T}}\boldsymbol{K}_2\boldsymbol{W}' + \delta\boldsymbol{W}'^{\mathrm{T}}\boldsymbol{K}_1\boldsymbol{W} + \delta\boldsymbol{W}^{\mathrm{T}}\boldsymbol{K}_1^{\mathrm{T}}\boldsymbol{W}' + \delta\boldsymbol{W}^{\mathrm{T}} \\ &\quad (\boldsymbol{K}_0 - \omega^2\boldsymbol{M})\boldsymbol{W} - \delta\boldsymbol{W}^{\mathrm{T}}\boldsymbol{F}]dx + \delta\boldsymbol{d}^{\mathrm{T}}\boldsymbol{f}_c = 0 \end{aligned} \tag{35}$$

where

$$\begin{aligned} \boldsymbol{f}_c &= \{-\boldsymbol{N}(0,\omega)\ -\boldsymbol{T}(0,\omega)\ \ \boldsymbol{N}(l,\omega)\ \ \boldsymbol{T}(l,\omega)\}^{\mathrm{T}} \\ &= \{\boldsymbol{N}_1(\omega)\ \boldsymbol{T}_1(\omega)\ \boldsymbol{N}_2(\omega)\ \boldsymbol{T}_2(\omega)\}^{\mathrm{T}} \end{aligned} \tag{36}$$

By substituting Eq. (33) into Eq. (35), the spectral element equation is obtained as

$$\boldsymbol{S}(\omega)\boldsymbol{d} = \boldsymbol{f}_c + \boldsymbol{f}_d \tag{37}$$

where $\boldsymbol{S}(\omega)$ is the (4N+6)-by-(4N+6) frequency dependent symmetric stiffness matrix often called spectral element matrix, defined by

$$\begin{aligned} \boldsymbol{S}(\omega) = \int_0^l &[\boldsymbol{N}'^{\mathrm{T}}\boldsymbol{K}_2\boldsymbol{N}' + (\boldsymbol{N}'^{\mathrm{T}}\boldsymbol{K}_1\boldsymbol{N} + \boldsymbol{N}^{\mathrm{T}}\boldsymbol{K}_1^{\mathrm{T}}\boldsymbol{N}') \\ &+ \boldsymbol{N}^{\mathrm{T}}(\boldsymbol{K}_0 - \omega^2\boldsymbol{M})\boldsymbol{N}]dx \end{aligned} \tag{38}$$

and $\boldsymbol{f}_d(\omega)$ is the spectral nodal force vector defined by

$$\boldsymbol{f}_d = \int_0^l \boldsymbol{N}(x;\omega)^{\mathrm{T}}\boldsymbol{Q}(x)\,dx \tag{39}$$

By substituting Eq. (34) into Eq. (38), the spectral element matrix can be rewritten in the following form

$$\boldsymbol{S}(\omega) = \boldsymbol{H}^{-\mathrm{T}}(\omega)\boldsymbol{D}(\omega)\boldsymbol{H}^{-1}(\omega) \tag{40}$$

where

$$\begin{aligned} \boldsymbol{D}(\omega) = [&\boldsymbol{R}^{\mathrm{T}}(\boldsymbol{K}_0 - \omega^2\boldsymbol{M})\boldsymbol{R} - \bar{\boldsymbol{k}}\boldsymbol{R}^{\mathrm{T}}\boldsymbol{K}_2\boldsymbol{R}\bar{\boldsymbol{k}} \\ &- i\bar{\boldsymbol{k}}(\boldsymbol{R}^{\mathrm{T}}\boldsymbol{K}_1\boldsymbol{R} + \boldsymbol{R}^{\mathrm{T}}\boldsymbol{K}_1^{\mathrm{T}}\boldsymbol{R})].*\boldsymbol{\Sigma} \\ \boldsymbol{\Omega} &= diagoanl[\Omega_q(\omega)] \end{aligned} \tag{41}$$

where the symbol (.*) denotes the "element-wise matrix multiplication" defined in MATLAB® (1993). The other symbols in Eq. (41) are defined by

$$\begin{aligned} &\Omega_q(\omega) = \int_0^l e^{-ik_q x}Q(x;\omega)dx \quad (q = 1,\ 2,\ 3,\ldots,\ 4N+6) \\ &\bar{\boldsymbol{k}} = diagonal[k_q] \quad (q = 1,\ 2,\ 3,\cdots,\ 4N+6) \\ &\boldsymbol{\Sigma} = \int_0^L \boldsymbol{E}(x;\omega)\boldsymbol{E}(x;\omega)dx = [\Sigma_{pq}] \quad (p,\ q = 1,\ 2,\ 3\ldots,\ 4N+6) \end{aligned} \tag{42}$$

where $Q(x;\omega)$ is the spectral component of the distributed axial force $q(x,t)$ acting on the outer surface of the axial bar and

$$\Sigma_{pq} = \begin{cases} \dfrac{i}{k_p + k_q}(e^{-i(k_p+k_q)l} - 1) & \text{if } k_p + k_q \neq 0 \\ l & \text{if } k_p + k_q = 0 \end{cases} \tag{43}$$

3.2 Spectral element analysis

Once the spectral element model represented by Eq. (37) has been derived, the spectral element analysis can be

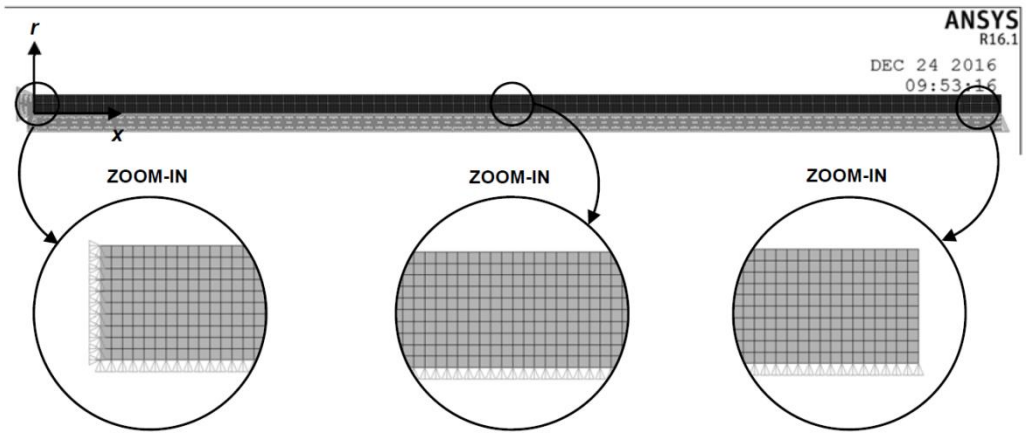

Fig. 3 The finite element mesh used for the example FGM bar: PLANE182 elements in ANSYS

Table 1 Comparison of the natural frequencies (Hz) of a fixed-free FGM bar (when m=1) obtained by the present SEM and by ANSYS

Mode number	SEM						ANSYS
	N = 1	N = 20	N = 50	N = 100	N = 150	N = 200	
1	3162.02	3161.66	3161.65	3161.65	3161.65	3161.65	3161.34
2	9484.80	9483.58	9483.56	9483.56	9483.56	9483.56	9482.51
3	15803.8	15801.3	15801.3	15801.3	15801.3	15801.3	15799.2
4	22116.5	22112.0	22112.0	22112.0	22112.0	22112.0	22108.2
5	28420.4	28413.0	28412.8	28412.8	28412.8	28412.8	28406.7
10	59712.9	59670.2	59669.2	59669.2	59669.2	59669.2	59629.6
20	119934	119687	119679	119679	119679	119679	119274
30	173844	172483	172449	172448	172448	172448	170197
40	218067	208529	208396	208392	208391	208391	201402

Note: N=The number of sub-layers in the inner (FGM) layer.

conducted in a straightforward manner as introduced in Lee (2009).

The structure under consideration can be discretized into multiple finite elements. Thus, the spectral element equations for each element should be assembled first by using the same methodology as used in the standard FEM. After imposing relevant boundary conditions, we obtain the global dynamic stiffness matrix equation in the following form:

$$\boldsymbol{S}_g(\omega)\boldsymbol{d}_g = \boldsymbol{f}_g \tag{44}$$

where the subscripts g denote the matrix and vectors for assembled global system.

First, the natural frequencies ω_N can be obtained from the condition that the determinant of $\boldsymbol{S}_g(\omega)$ must vanish at $\omega = \omega_N$. Second, the dynamic responses in the frequency domain or the frequency response functions can be readily computed from $\boldsymbol{d}_g = \boldsymbol{S}_g(\omega)^{-1}\boldsymbol{f}_g$. Last, the dynamic responses in the time domain (or the time histories of displacements and slopes) can be efficiently computed from Eq. (19) via Eq. (32) by using an inverse fast Fourier transform (FFT) algorithm.

4. Numerical results and discussion

In our numerical studies, we considered a three-layer FGM bar that is uniform in the axial direction and has the following geometry: the length l=0.5 m, the radius of the outer layer r_O=0.01 m, the radius of the inner FGM layer r_I=0.009 m, and the radius of the core r_C=0.001 m. The core of the FGM bar is made of alumina (Al_2O_3) and its material properties are E_I=390 GPa and ρ_C=3950 kg/m. The outer layer is made of mild steel and its material properties are E_O=210 GPa and ρ_O=7800 kg/m^3 (Chakraborty and Gopalakrishinan 2003, Hong *et al.* 2014, Hong and Lee 2015). Young's modulus and the mass density in the inner FGM layer are determined by the power law given by Eq. (7). We assumed that the left end of the FGM bar (x=0) is fixed and the right end of the FGM bar (x=L) is free.

To validate the high accuracy of the present spectral element model (denoted by "SEM"), the natural frequencies (in Hertz) and the frequency response functions (FRF) obtained by the present SEM were compared with those obtained by using the commercial finite element analysis package ANSYS (2006). We assumed that the power law exponent m is equal to 1, and the core, inner layer, and outer layer have the same Poisson's ratio ($\nu_C = \nu_I = \nu_O$ = 0.3). To obtain the FRFs, an axisymmetric circular unit impulse was applied at the middle of the inner FGM layer (at $r = (r_C+r_I)/2$). The dynamic responses of axial displacement were computed at the middle of the inner FGM layer. For the ANSYS analysis, an axisymmetric 2-D four-node structural solid element (called the PLANE182 element) was used (see Fig. 3). The total number of finite elements used in the ANSYS analysis was increased to more than 2×10^7 until sufficiently converged results were obtained. For the SEM results, the number of sub-layers in the inner FGM layer (denoted by N) was increased step-by-step to N = 120. Table 1 shows that the SEM results approach the ANSYS results as the number of sub-layers in the inner FGM layer is increased. Figure 4 also shows that the FRFs obtained by the present SEM approach the ANSYS results as the number of sub-layers in the inner FGM layer is increased. For this axial bar subjected to fixed-free boundary conditions, the present SEM has nodes only on the cross-section of the free end, but no nodes inside the

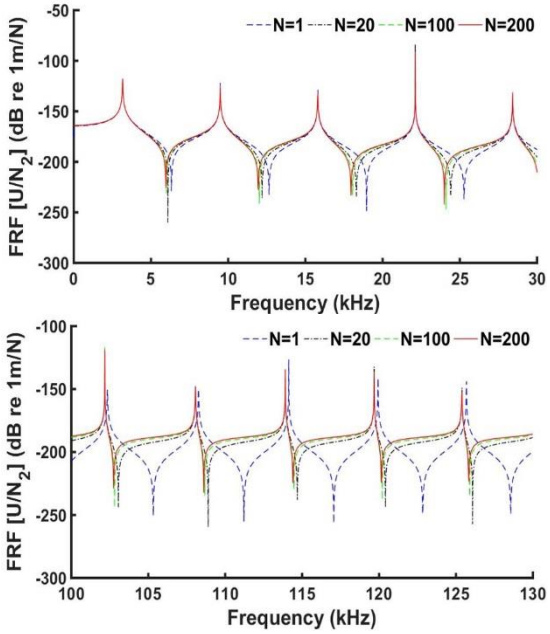

Fig. 4 Effects of the number of sub-layers in the inner FGM layer (N) on the frequency response functions (FRFs) of a fixed-free FGM bar (when m=1) obtained by the present SEM

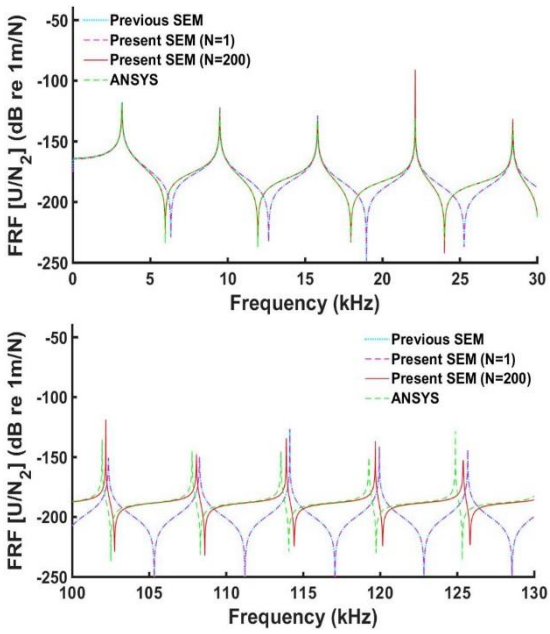

Fig. 5 Comparison of the frequency response functions (FRFs) of a fixed-free FGM bar (when m=1) obtained by the previous SEM (Hong and Lee 2015), the present SEM, and ANSYS

FGM bar. Thus, we suggest that, compared to the ANSYS finite element analysis results, the present SEM provides very accurate results by using only an extremely small number of DOFs.

In the previous study by Hong and Lee (2015), the radial displacements in each layer of an FGM bar were assumed to vary linearly in the radial direction. However, this might not be true as the radial displacements in the inner FGM layer will not vary linearly due to the radial variation of material properties. Thus, in the present study, the inner FGM layer was divided into N sub-layers to improve the accuracy of the three-layer axial bar model. Accordingly, the present spectral element model (hereafter called "present SEM") with N=1 corresponds to the spectral element model considered in Hong and Lee (2015) (hereafter called "previous SEM")

To compare the present SEM with the previous SEM, the FRFs and natural frequencies obtained by the present SEM and the previous SEM (Hong and Lee 2015) are compared in Fig. 5 and Table 2, respectively. As expected, Fig. 5 and Table 2 show that the FRFs and natural frequencies obtained by the present SEM when N=1 are identical to those obtained by the previous SEM (Hong and Lee 2015). However, as we increase the number of sub-layers in the inner FGM layer up to about N=200, the accuracy of the present SEM is improved so that the SEM results approach the ANSYS results, as shown in Fig. 5 and Table 2. Thus, for the SEM results used to investigate the effects of Poisson's ratios and the power law exponent m on the dynamic characteristics of the example FGM bars, the number of sub-layers in the inner FGM layer was chosen as N=200.

Fig. 6 shows the effects of the Poisson's ratio of the inner FGM layer, ν_I, on the natural frequencies of the

Table 2 Comparison of the natural frequencies (Hz) of a fixed-free FGM bar (when m = 1) obtained by the previous SEM (Hong and Lee 2015) and the present SEM

Mode number	Previous SEM	Present SEM			
		N = 1	N = 20	N = 100	N = 200
1	3162.02	3162.02	3161.66	3161.65	3161.65
2	9484.80	9484.80	9483.58	9483.56	9483.56
3	15803.8	15803.8	15801.3	15801.3	15801.3
4	22116.5	22116.5	22112.0	22112.0	22112.0
5	28420.4	28420.4	28412.9	28412.8	28412.8
10	59712.9	59712.9	59669.5	59669.2	59669.2
20	119934	119934	119681	119679	119679
30	173844	173844	172457	172448	172448
40	218067	218067	208426	208392	208391

Note: N=The number of sublayers in the inner (FGM) layer.

example fixed-free FGM bar for three values of the power law exponent (m=0.5, 1, and 2). The Poisson's ratios of the core and the outer layer (ν_C and ν_O) were assumed to be ν_C=ν_O=0.3. Fig. 7 shows the effects of the power law exponent n on the natural frequencies of the fixed-free FGM bar for three values of ν_I (ν_I=0.2, 0.3, and 0.4). From Figs. 6 and 7, we note the following: (1) For a fixed value of the power law exponent m, the natural frequencies above the fiftieth mode become larger as Poisson's ratio ν_I increases, while the natural frequencies below the fortieth mode become smaller; (2) For a fixed value of Poisson's ratio ν_I, all natural frequencies seem to increase as the power law exponent m increases; (3) In general, the natural frequency of the example fixed-free FGM bar steadily increases as the mode number increases to about 40, but it changes very slowly as the mode number increases beyond

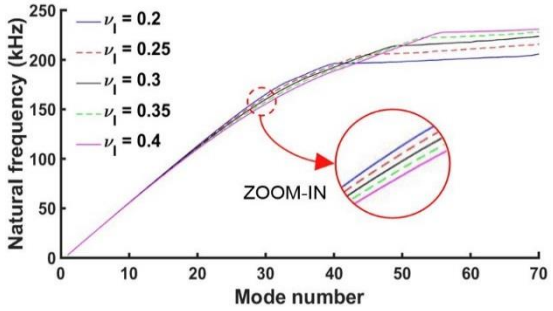

(a) when m=0.5

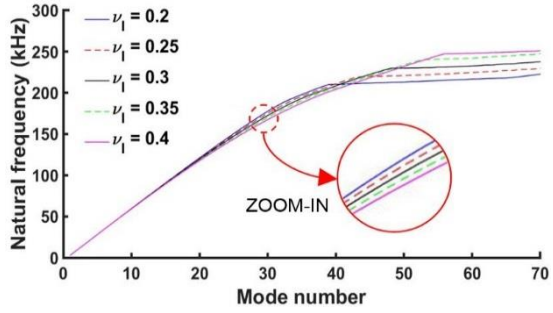

(b) when m=1

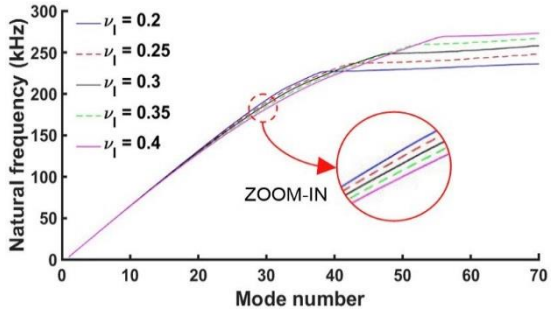

(c) when m=2

Fig. 6 Effects of Poisson's ratio of the inner FGM layer (ν_I) on the natural frequencies of a fixed-free FGM bar for three different values of the power law exponent (m)

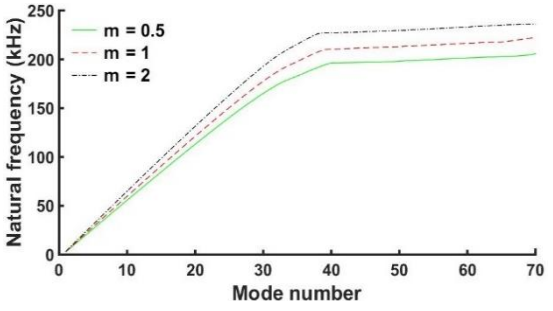

(a) when ν_I=0.2

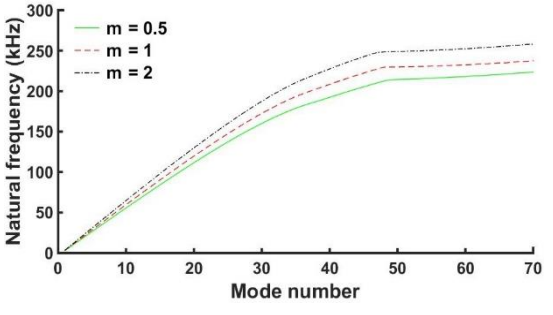

(b) when ν_I=0.3

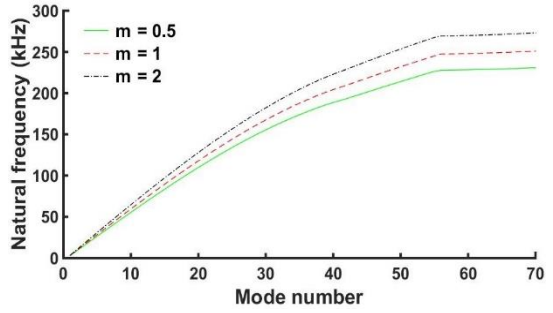

(c) when ν_I=0.4

Fig. 7 Effects of the power law exponent (m) on the natural frequencies of a fixed-free FGM bar for three values of Poisson's ratio of the inner FGM layer (ν_I)

about 40, regardless of the changes of the power law exponent m and Poisson's ratio ν_I.

Fig. 8 shows a comparison of the dynamic responses obtained by the present SEM, the previous SEM (Hong and Lee 2015), and ANSYS (2006) when an excitation axial force in the form of a five-peak Morlet-wavelet input signal (with a center frequency of 100 kHz) was applied at the interface between the core and the inner FGM layer at x=L (free end) of the example fixed-free FGM bar. Fig. 8(a) shows the dynamic responses $U_1(L, t)$, $U_{N/2+1}(L, t)$, and $U_{N+1}(L, t)$ obtained at the interface between the core and the inner FGM layer, at the middle sub-layer in the inner FGM layer, and at the interface between the inner FGM layer and the outer layer, respectively, at x=L of the FGM bar. Similarly, Fig. 8(b) shows the dynamic responses obtained at the same three locations in the radial direction at the middle of the FGM bar (x=L/2) shown in Fig. 8(a).

From Fig. 8, we note the following: (1) The dynamic responses obtained by the present SEM are almost identical to those obtained by using ANSYS (2006); (2) The dynamic responses obtained by the present SEM are quite different from those obtained by the previous SEM (Hong and Lee 2015), especially in the early stage of the dynamic responses (from t=0 to 0.05 ms). The discrepancy is significant near the excitation point, but becomes less significant as the distance from the excitation point increases in the radial direction or in the axial direction. This phenomenon is described by Saint-Venant's principle (Timoshenko and Goodier 1934).

Fig. 9 shows a comparison of the wave propagations in the example fixed-free FGM bar obtained by the present SEM and the previous SEM (Hong and Lee 2015). To generate wave propagations in the FGM bar, the same excitation axial force as considered for Fig. 9 was applied at the interface between the core and the inner FGM layer at the free end of the example FGM bar. The wave propagations were obtained at three locations in the radial directions: $U_1(x, t)$ at the interface between the core and the inner FGM layer, $U_{N/2+1}(x, t)$ at the middle sub-layer in the inner FGM layer, and $U_{N+1}(x, t)$ at the interface between the

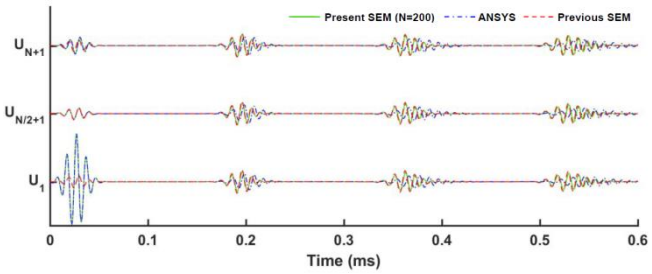

(a) at $x=L$

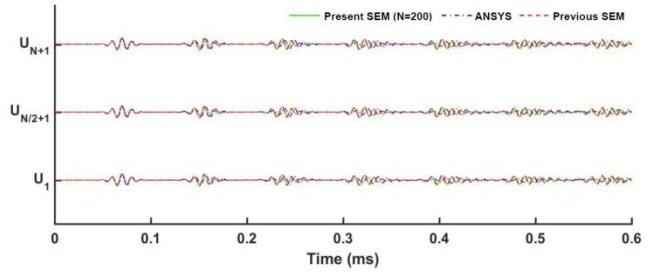

(b) at $x=L/2$

Fig. 8 Comparison of the dynamic responses at (a) the free end ($x=L$) and (b) the middle ($x=L/2$) of the fixed-free FGM bar obtained by the present SEM, the previous SEM (Hong and Lee 2015), and ANSYS when an excitation axial force in the form of a five-peak Morlet-wavelet input signal is applied at the free end

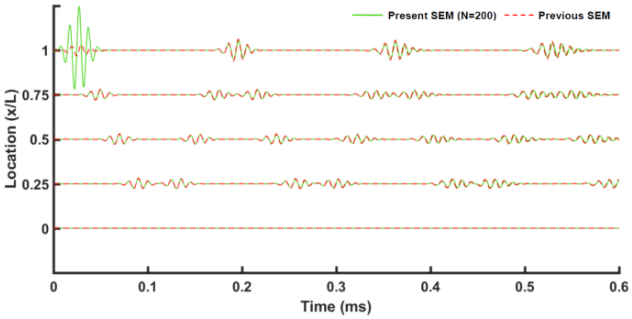

(a) $U_1(x,t)$

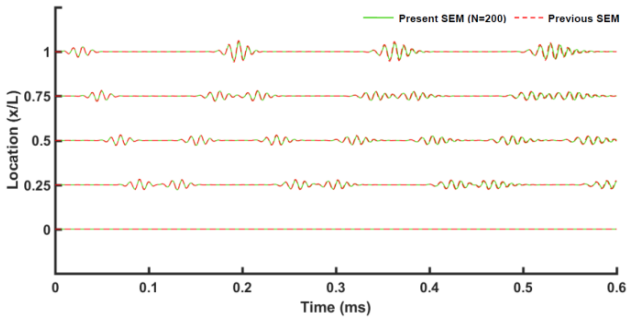

(b) $U_{N/2+1}(x,t)$

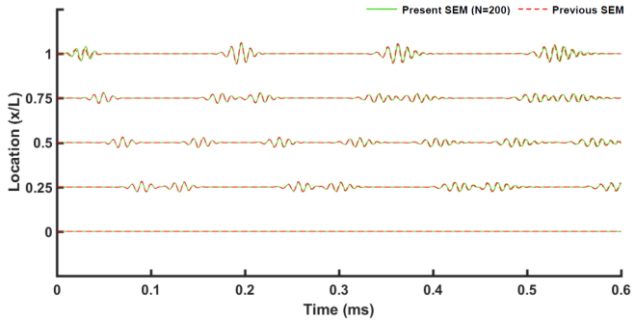

(c) $U_{N+1}(x,t)$

Fig. 9 Comparison of the wave propagations at three locations in the radial direction obtained by the present SEM and the previous SEM (Hong and Lee 2015) when an excitation axial force that has the form of a five-peak Morlet-wavelet input signal is applied at the free end ($x=L$) of the fixed-free FGM bar

inner FGM layer and the outer layer. Fig. 9 also shows that the discrepancy between the wave propagations obtained by the present SEM and the previous SEM (Hong and Lee 2015) is most significant near the excitation point, but becomes less significant as the distance from the excitation point increases in the radial direction or in the axial direction due to Saint-Venant's principle (Timoshenko and Goodier 1934).

5. Conclusions

We propose an enhanced spectral element model for three-layered FGM bars. The FGM bar model proposed in the previous work by Hong and Lee (2015) was improved by treating axial and radial displacements in the radial direction more realistically by representing the inner FGM layer with multiple sub-layers. The Young's modulus and mass density of the inner FGM layer were assumed to vary in the radial direction according to the power law. The spectral element model was then formulated by using the variational approach. The accuracy and performance of the proposed enhanced spectral element model were evaluated by comparison with solutions obtained by the commercial finite element package ANSYS. Based on the numerical results obtained in this study, the following conclusions are made:

(1) To accurately predict the natural frequencies and frequency response functions up to a high frequency, we recommend the present SEM, instead of using the previous SEM by Hong and Lee (2015).

(2) To accurately predict the dynamic responses or wave propagations at or near the excitation point, the inner FGM layer must be represented by multiple sub-layers as in the present SEM, rather than representing it as a single layer as in the previous SEM by Hong and Lee (2015).

(3) The dynamic responses or wave propagations at a distance sufficiently far from the excitation point can be well predicted by using the previous SEM by Hong and Lee (2015), which is justified by Saint-Venant's principle (Timoshenko and Goodier 1934).

Acknowledgements

This research was supported by the Inha University research grant.

References

ANSYS Release 11.0 (2006), Documentation for ANSYS, ANSYS, Inc, Canonsburg, PA, USA.

Chakraborty, A. and Gopalakrishinan, S. (2003), "A spectrally formulated finite element for wave propagation in functionally graded beams", *Int. J. Solid. Struct.*, **40**(10), 2421-2448.

Efraim, E. and Eisenberger, M. (2007), "Exact solution analysis of variable thickness thick annular isotropic and FGM plates", *J. Sound Vib.*, **299**(4-5), 720-738.

Hong, M., Park, I. and Lee, U. (2014), "Dynamics and waves characteristics of the FGM axial bars by using spectral element method", *Compos. Struct.*, **107**, 585-593.

Hong, M. and Lee, U. (2015), "Dynamics of a functionally graded material axial bar: spectral element modeling and analysis", *Compos. Part B-Eng.*, **69**, 427-434.

Horgan, C.O. (1999), "The pressurized hollow cylinder or disk problem for functionally graded isotropic linearly elastic materials", *J. Elasticity*, **55**(1), 43-59.

Horgan, C.O. (2007), "On the torsion of functionally graded anisotropic linearly elastic bars", *IMA J. Appl. Math.*, **72**(5), 556-562.

Huang, Y. and Li, X.F. (2010), "A new approach for free vibration of axially functionally graded beams with non-uniform cross-section", *J. Sound Vib.*, **329**(11), 2291-2303.

Kreyszig, E. (1972), *Advanced Engineering Mathematics*, John Wiley & Sons, New York.

Kutis, V. and Murin, J. (2006), "Stability of slender beam-column with locally varying Young's modulus", *Struct. Eng. Mech.* **23**(1), 15-27

Lee, U. (2009), *Spectral Element Method in Structural Dynamics*, John Wiley & Sons, Singapore.

Li, X.F. (2008), "A unified approach for analyzing static and dynamic behavior of functionally graded Timoshenko and Euler-Bernoulli beams", *J. Sound Vib.* **318**(4-5), 1210-1229.

Maalawi, K.Y. (2011), "Functionally graded bars with enhanced dynamic performance", *J. Mech. Mater. Struct.*, **6**(1-4), 377-393.

Markworth, A.J., Ramesh, K.S. and Parks Jr., W.P. (1995), "Modeling studies applied to functionally graded materials", *J. Mater. Sci.*, **30**(9), 2183-2193.

Mashat, D.S., Carrera, E., Zenkour, A.M., Khateeb, S.A.A. and Filippi, M. (2014), "Free vibration of FGM layered beams by various theories and finite elements", *Compos. Part B-Eng.*, **59**, 269-278.

MATLAB User's Guide (1993), MathWorks, Natick, MA, USA.

Meirovitch, L. (1967), *Analytical Methods in Vibrations*, Macmillan, London.

Menaa, R., Tounsi, A., Mouaici, F., Mechab, I., Zidi, M. and Bedia, E.A.A. (2012), "Analytical solutions for static shear correction factor of functionally graded rectangular beams", *Mech. Adv. Mater. Struct.*, **19**(8), 641-652.

Murin, J., Aminbaghai, M., Hrabovsky, J., Kutis, V. and Kugler, S. (2013), "Modal analysis of the FGM beams with effect of the shear correction function", *Compos. Part B-Eng.*, **45**(1), 1575-1582.

Murin, J., Aminbaghai, M., Hrabovsky, J., Gogola, R. and Kugler, S. (2016), "Beam finite element for modal analysis of FGM structures", *Eng. Struct*., **121**, 1-18.

Murin, J., Kutis, V. and Masny, M. (2008), "An effective solution of electro-thermo-structural problem of uni-axially graded material", *Struct. Eng. Mech*., **28**(6), 695 -713.

Murin, J., Kutis, V., Paulech, J. and Hrabovsky, J. (2011), "Electric-thermal link finite element made of FGM with spatially variation of material properties", *Compos. Part B-Eng*., 42, 1966-1979.

Newland, D.E. (1993), *Random Vibrations: Spectral and Wavelet Analysis*, Longman, New York.

Nguyen, T.K., Vo, T.P. and Thai, H.T. (2013), "Static and free vibration of axially loaded functionally graded beams based on the first-order shear deformation theory", *Compos. Part B-Eng.*, **55**, 147-157.

Parker, D.F. (2009), "Waves and statics for functionally graded materials and laminates", *Int. J. Eng. Sci.*, **47**(11-12), 1315-1321.

Pradhan, K.K. and Chakraverty, S. (2013), "Free vibration of Euler and Timoshenko functionally graded beams by Rayleigh-Ritz method", *Compos. Part B-Eng.*, **51**, 175-184.

Shahba, A., Attarnejad, R. and Hajilar, S. (2011), "Free vibration and stability of axially functionally graded tapered Euler-Bernoulli beams", *Shock Vib.*, **18**(5), 683-696.

Timoshenko, S.P. and Goodier, J.N. (1934), *Theory of Elasticity*, McGraw-Hill, New York.

Xiang, H.J. and Yang, J. (2008), "Free and forced vibration of a laminated FGM Timoshenko beam of variable thickness under heat conduction", *Compos. Part B-Eng.*, **39**(2), 292-303.

Yu, Z. and Chu, F. (2009), "Identification of crack in functionally graded material beams using the *p*-version of finite element method", *J. Sound. Vib.*, **325**(1-2), 69-84.

CC

Appendix: Effective mass and stiffness matrices

(1) Effective mass matrices:

$$\boldsymbol{M}_{uu} = 2\pi\int_{r_C}^{r_I} r\rho_I(r)\boldsymbol{R}_{uI}^{\mathrm{T}}(r)\boldsymbol{R}_{uI}(r)dr + \boldsymbol{m}_{uu},$$

$$\boldsymbol{M}_{\psi\psi} = 2\pi\int_{r_C}^{r_I} r\rho_I(r)\boldsymbol{R}_{vI}^{\mathrm{T}}(r)\boldsymbol{R}_{vI}(r)dr + \boldsymbol{m}_{\psi\psi} \quad \text{(A.1)}$$

where

$$\boldsymbol{m}_{uu} = \begin{bmatrix} \rho_C A_C & 0 & 0 & \cdots & 0 & 0 \\ 0 & 0 & 0 & \cdots & 0 & 0 \\ 0 & 0 & 0 & \cdots & 0 & 0 \\ \vdots & \vdots & \vdots & \ddots & \vdots & \vdots \\ 0 & 0 & 0 & \cdots & 0 & 0 \\ 0 & 0 & 0 & \cdots & 0 & \rho_O A_O \end{bmatrix}$$

$$\boldsymbol{m}_{\psi\psi} = \begin{bmatrix} \eta_0 + \Delta r_0\Delta r_0\eta_1 & \Delta r_0\Delta r_1\eta_1 & \Delta r_0\Delta r_2\eta_1 & \cdots & \Delta r_0\Delta r_N\eta_1 & \Delta r_0\eta_2 \\ \Delta r_0\Delta r_1\eta_1 & \Delta r_1\Delta r_1\eta_1 & \Delta r_1\Delta r_2\eta_1 & \cdots & \Delta r_1\Delta r_N\eta_1 & \Delta r_1\eta_2 \\ \Delta r_0\Delta r_2\eta_1 & \Delta r_1\Delta r_2\eta_1 & \Delta r_2\Delta r_2\eta_1 & \cdots & \Delta r_2\Delta r_N\eta_1 & \Delta r_2\eta_2 \\ \vdots & \vdots & \vdots & \ddots & \vdots & \vdots \\ \Delta r_0\Delta r_N\eta_1 & \Delta r_1\Delta r_N\eta_1 & \Delta r_2\Delta r_N\eta_1 & \cdots & \Delta r_N\Delta r_N\eta_1 & \Delta r_N\eta_2 \\ \Delta r_0\eta_2 & \Delta r_1\eta_2 & \Delta r_2\eta_2 & \cdots & \Delta r_N\eta_2 & \eta_3 \end{bmatrix} \quad \text{(A.2)}$$

and where the following definitions are used

$$A_C = \pi r_C^2,\ A_O = \pi(r_O^2 - r_I^2),\ J_C = \frac{1}{2}\pi r_C^4$$

$$\eta_0 = \rho_C J_C,\ \eta_1 = \rho_O A_O,\ \eta_2 = \frac{\pi}{3}\mu_O(2r_O + r_I)\Delta r_{N+1}^2$$

$$\eta_3 = \frac{\pi}{6}\rho_O(3r_O + r_I)\Delta r_{N+1}^3 \quad \text{(A.3)}$$

(2) Effective stiffness matrices:

$$\boldsymbol{K}_{u'u'} = 2\pi\int_{r_C}^{r_I} r[\{\lambda_I(r) + 2\mu_I(r)\}\boldsymbol{R}_{uI}^{\mathrm{T}}(r)\boldsymbol{R}_{uI}(r)]dr + \boldsymbol{\kappa}_{u'u'}$$

$$\boldsymbol{K}_{uu} = 2\pi\int_{r_C}^{r_I} r\mu_I(r)\boldsymbol{R}_{uI,r}^{\mathrm{T}}(r)\boldsymbol{R}_{uI,r}(r)dr$$

$$\boldsymbol{K}_{u'\psi} = 2\pi\int_{r_C}^{r_I} \lambda_I(r)[r\boldsymbol{R}_{uI}^{\mathrm{T}}(r)\boldsymbol{R}_{vI,r}(r) + \boldsymbol{R}_{uI}^{\mathrm{T}}(r)\boldsymbol{R}_{vI}(r)]dr + \boldsymbol{\kappa}_{u'\psi}$$

$$\boldsymbol{K}_{\psi'u} = 2\pi\int_{r_C}^{r_I} r\mu_I(r)\boldsymbol{R}_{vI}^{\mathrm{T}}(r)\boldsymbol{R}_{uI,r}(r)dr \quad \text{(A.4)}$$

$$\boldsymbol{K}_{\psi'\psi'} = 2\pi\int_{r_C}^{r_I} r\mu_I(r)\boldsymbol{R}_{vI}^{\mathrm{T}}(r)\boldsymbol{R}_{vI}(r)dr + \boldsymbol{\kappa}_{\psi'\psi'}$$

$$\boldsymbol{K}_{\psi\psi} = 2\pi\int_{r_C}^{r_I} [\{\lambda_I(r) + 2\mu_I(r)\}\{r\boldsymbol{R}_{vI,r}^{\mathrm{T}}(r)\boldsymbol{R}_{vI,r}(r) + r^{-1}\boldsymbol{R}_{vI}^{\mathrm{T}}(r)\boldsymbol{R}_{vI}(r)\} + \lambda_I(r)\{\boldsymbol{R}_{vI}^{\mathrm{T}}(r)\boldsymbol{R}_{vI,r}(r) + \boldsymbol{R}_{vI,r}^{\mathrm{T}}(r)\boldsymbol{R}_{vI}(r)\}]dr + \boldsymbol{\kappa}_{\psi\psi}$$

where

$$\boldsymbol{\kappa}_{u'u'} = \begin{bmatrix} (\lambda_C + 2\mu_C)A_C & 0 & 0 & \cdots & 0 & 0 \\ 0 & 0 & 0 & \cdots & 0 & 0 \\ 0 & 0 & 0 & \cdots & 0 & 0 \\ \vdots & \vdots & \vdots & \ddots & \vdots & \vdots \\ 0 & 0 & 0 & \cdots & 0 & 0 \\ 0 & 0 & 0 & \cdots & 0 & (\lambda_O + 2\mu_O)A_O \end{bmatrix}$$

$$\boldsymbol{\kappa}_{u'\psi} = \begin{bmatrix} 2\lambda_C A_C & 0 & \cdots & 0 & 0 & 0 \\ 0 & 0 & \cdots & 0 & 0 & 0 \\ \vdots & \vdots & \ddots & \vdots & \vdots & \vdots \\ 0 & 0 & \cdots & 0 & 0 & 0 \\ \alpha\Delta r_0 & \alpha\Delta r_1 & \cdots & \alpha\Delta r_{N-1} & \alpha\Delta r_N & \alpha r_O \end{bmatrix} \quad \text{(A.5)}$$

$$\boldsymbol{\kappa}_{\psi'\psi'} = \begin{bmatrix} \beta_0 + \Delta r_0\Delta r_0\beta_1 & \Delta r_0\Delta r_1\beta_1 & \Delta r_0\Delta r_2\beta_1 & \cdots & \Delta r_0\Delta r_N\beta_1 & \Delta r_0\beta_2 \\ \Delta r_0\Delta r_1\beta_1 & \Delta r_1\Delta r_1\beta_1 & \Delta r_1\Delta r_2\beta_1 & \cdots & \Delta r_1\Delta r_N\beta_1 & \Delta r_1\beta_2 \\ \Delta r_0\Delta r_2\beta_1 & \Delta r_1\Delta r_2\beta_1 & \Delta r_2\Delta r_2\beta_1 & \cdots & \Delta r_2\Delta r_N\beta_1 & \Delta r_2\beta_2 \\ \vdots & \vdots & \vdots & \ddots & \vdots & \vdots \\ \Delta r_0\Delta r_N\beta_1 & \Delta r_1\Delta r_N\beta_1 & \Delta r_2\Delta r_N\beta_1 & \cdots & \Delta r_N\Delta r_N\beta_1 & \Delta r_N\beta_2 \\ \Delta r_0\beta_2 & \Delta r_1\beta_2 & \Delta r_2\beta_2 & \cdots & \Delta r_N\beta_2 & \beta_3 \end{bmatrix}$$

$$\boldsymbol{\kappa}_{\psi\psi} = \begin{bmatrix} \gamma_0 + \Delta r_0\Delta r_0\gamma_1 & \Delta r_0\Delta r_1\gamma_1 & \Delta r_0\Delta r_2\gamma_1 & \cdots & \Delta r_0\Delta r_N\gamma_1 & \Delta r_0\gamma_2 \\ \Delta r_1\Delta r_0\gamma_1 & \Delta r_1\Delta r_1\gamma_1 & \Delta r_1\Delta r_2\gamma_1 & \cdots & \Delta r_1\Delta r_N\gamma_1 & \Delta r_1\gamma_2 \\ \Delta r_2\Delta r_0\gamma_1 & \Delta r_2\Delta r_1\gamma_1 & \Delta r_2\Delta r_2\gamma_1 & \cdots & \Delta r_2\Delta r_N\gamma_1 & \Delta r_2\gamma_2 \\ \vdots & \vdots & \vdots & \ddots & \vdots & \vdots \\ \Delta r_N\Delta r_0\gamma_1 & \Delta r_N\Delta r_1\gamma_1 & \Delta r_N\Delta r_2\gamma_1 & \cdots & \Delta r_N\Delta r_N\gamma_1 & \Delta r_N\gamma_2 \\ \Delta r_0\gamma_2 & \Delta r_1\gamma_2 & \Delta r_2\gamma_2 & \cdots & \Delta r_N\gamma_2 & \gamma_3 \end{bmatrix}$$

and where the following definitions are used:

$$\alpha = 2\pi(r_O - r_I),\ \beta_0 = \mu_C J_C,\ \beta_1 = \mu_O A_O$$
$$\beta_2 = (\pi/3)\mu_O(2r_O + r_I)\Delta r_{N+1}^2,\ \beta_3 = (\pi/6)\mu_O(3r_O + r_I)\Delta r_{N+1}^3$$
$$\gamma_0 = 4(\lambda_C + \mu_c)A_C,\ \gamma_1 = 2\pi(\lambda_O + 2\mu_O)\log(r_O/r_I)$$
$$\gamma_2 = r_I\gamma_1 + 4\pi(\lambda_O + \mu_O)\Delta r_{N+1},\ \gamma_3 = (r_I^2\gamma_1/2) + \pi(3\lambda_O + 2\mu_O)\Delta r_{N+1}^2 \quad \text{(A.6)}$$